EDGE ARTICLE

Check for updates

All publication charges for this article have been paid for by the Royal Society of Chemistry

Strengthened π-type interaction in layered oxide cathodes with reversible anionic redox for sodium-ion batteries†

Zheng Zhou,[a] Chen Cheng,[a] Shuyuan Chen,[a] Tong Chen,[a] Lei Wang,[a] Tianran Yan,[a] Weidong Xu,[a] Shiqi Shen,[a] Jianrong Zeng[*b] and Liang Zhang [ID] [*ac]

Activating anionic redox activity in P2-type layered oxide cathodes is a promising pathway to enhance the specific capacity for sodium-ion batteries (SIBs). However, the highly active anionic redox process arising from the non-bonding O 2p orbitals frequently leads to irreversible oxygen release and surface degradation, which severely limit the long-term cycling stability. Herein, we propose a strategy of strengthening transition metal–oxygen (TM–O) π-type interaction with a regulated local oxygen coordination environment by incorporating the Ru^{4+}/Ru^{5+} redox couple into P2-type $Na_{0.6}Li_{0.2}Mn_{0.8}O_2$ (NLMO) to achieve a reversible anionic redox reaction. Upon high-voltage charging, the formed Ru^{5+} state with a half-filled t_{2g} $4d^3$ electronic configuration establishes a strengthened π-type interaction with non-bonding O 2p orbitals within the Na–O–Li configuration compared to the inherently weaker Mn–O π-type interaction in NLMO. Such a strengthened π-type interaction effectively enhances anionic redox reversibility, suppresses irreversible oxygen release and realizes a complete solid-solution behavior with stable TMO_6 octahedra throughout cycling. This preserved structural integrity also prevents crack formation and minimizes transition metal dissolution, thereby mitigating surface degradation. The resulting $Na_{0.6}Li_{0.2}Mn_{0.7}Ru_{0.1}O_2$ (NLMRO) thus exhibits a reversible anionic redox activity with markedly improved cycling stability. Our work highlights that dynamically engineering potent π-type interaction during electrochemical cycling is a promising avenue for developing high-performance SIBs with cumulative cationic and anionic redox reactions.

Introduction

The incorporation of an anionic redox reaction into layered oxide cathodes to provide extra capacity has been recognized as a viable approach for the development of high-energy-density sodium-ion batteries (SIBs).[1–5] A series of layered oxide cathodes, such as $Na_{0.6}Li_{0.2}Mn_{0.8}O_2$,[6] $Na_{0.78}Ni_{0.23}Mn_{0.69}\square_{0.08}O_2$ ($\square$: transition metal vacancy),[7] and $Na_{0.67}Mg_{0.72}Mn_{0.28}O_2$,[8] have demonstrated anionic redox activity during the electrochemical process of SIBs, which is primarily attributed to the formation of non-bonding O 2p orbitals resulting from a specific local configuration like Na–O–A (A stands for Na, Li and other elements with no covalent interaction with oxygen) or Na–O–$\square$ configurations.[9,10] Because these non-bonding O 2p orbitals

usually lie close to the Fermi level, their labile electrons can be easily removed to provide extra capacity during the electrochemical processes. However, this highly active anionic redox reaction resulting from the non-bonding O 2p orbitals frequently induces excessive oxygen oxidation and subsequent irreversible oxygen release, which could lead to irreversible transition metal (TM) migration due to decreased coordinating oxygen atoms after O_2 release.[11,12] Additionally, irreversible anionic redox occurring at high voltages has been reported to induce distorted TMO_6 octahedra with a destabilized oxygen framework,[13] which could result in undesirable structural distortions and phase transitions.[14] This is frequently accompanied by the formation of surface cracks and detrimental surface side reactions (*e.g.*, TM dissolution), thereby hindering further application of the anionic redox reaction in layered oxide cathodes (Fig. 1a). Therefore, effective regulation of the anionic redox reaction is indispensable for achieving high-performance SIBs.

To address aforementioned issues, enhancing the overall TM–O covalency or employing different dopants to mitigate oxygen release and structural distortion has been extensively reported.[15,16] However, these approaches have inherent limitations. For example, increasing TM–O covalency inadvertently

[a]*Institute of Functional Nano & Soft Materials (FUNSOM), Soochow University, Suzhou 215123, Jiangsu, China. E-mail: liangzhang2019@suda.edu.cn*

[b]*Shanghai Synchrotron Radiation Facility, Shanghai Advanced Research Institute, Chinese Academy of Sciences, Shanghai 201204, China. E-mail: zengjr@sari.ac.cn*

[c]*Jiangsu Key Laboratory of Advanced Negative Carbon Technologies, Soochow University, Suzhou 215123, China*
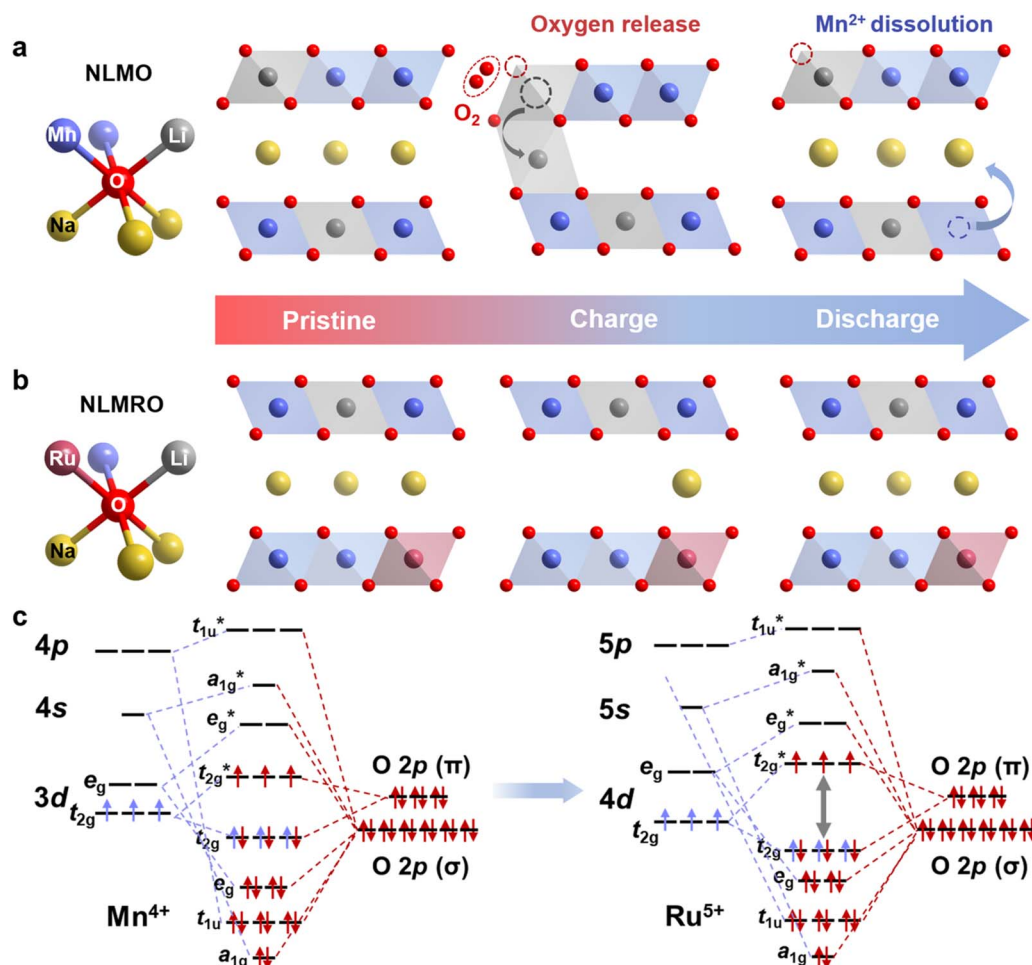
Fig. 1 Proposed strategy for strengthening π-type interaction. Schematic illustration of structural evolution in (a) NLMO and (b) NLMRO upon cycling. (c) Molecular orbital energy diagrams of MnO_6 octahedra in NLMO and RuO_6 octahedra in NLMRO.

sacrifices certain anionic redox activity by lowering the energy of O 2p states,[17] while doping with electrochemically inactive elements (*e.g.*, Mg and Zn) inevitably reduces the specific capacity of cathode materials.[18] On the other hand, these approaches largely overlooked the specific nature and orbital symmetry requirements of the underlying TM–O electronic interactions that govern the oxygen redox stability. Intriguingly, recent investigations emphasized that the anionic redox behavior is acutely sensitive to the local oxygen environment, and more specifically the precise character of these TM–O interactions. For example, Kang *et al.* highlighted that the local environment of oxygen undergoes different changes through σ- or π-type interaction.[19] Fundamentally, the O 2p orbitals directly hybridize with the d orbitals of adjacent TM atoms in σ-type interaction. However, the O 2p orbitals along the Na–O–Li/ □ axis exhibit a penchant for hybridizing with TM t_{2g} orbitals in a shoulder-to-shoulder manner, especially in the case of TM atoms with a d^3 (t_{2g}^3) or d^6 (t_{2g}^6) electronic configuration,[20] resulting in the formation of π-type interaction.[21] Such π-type interaction could induce the TM–O hybridization orbitals to split into π-type bonding and anti-bonding orbitals. During the anionic redox process, electrons are preferentially removed

from the higher-energy anti-bonding orbitals, which further enhances the orbital splitting and stabilizes the oxidized oxygen with enhanced reversibility.[22,23] However, it is worth mentioning that it has been mainly focused on the construction/regulation of π-type interaction for the pristine materials,[24,25] but the electronic configuration of TM atoms and thus the interaction with oxygen for constructing π-type interaction is not static during battery operation. Therefore, instead of relying on a fixed pristine state, alternative strategies that dynamically construct or considerably enhance the π-type interaction during the cycling process are critical for achieving reversible anionic redox reactions in layered oxide cathodes.

Herein, we propose a strategy of strengthening π-type interaction over cycling by introducing a reversible Ru^{4+}/Ru^{5+} redox couple into P2-type $Na_{0.6}Li_{0.2}Mn_{0.8}O_2$ (NLMO) to achieve $Na_{0.6}Li_{0.2}Mn_{0.7}Ru_{0.1}O_2$ (NLMRO) with enhanced structural stability and anionic redox reversibility. The Ru^{5+} state with a $4d^3$ configuration of t_{2g} orbitals formed before the onset of anionic redox results in strengthened π-type interaction with non-bonding O 2p orbitals within the Na–O–Li configuration compared to the Mn–O π-type interaction in NLMO considering the TM electronegativity and energy level of the t_{2g} orbital

relative to the O 2p energy level (Fig. 1c).[21] The enhanced Ru–O π-type interaction could not only effectively enhance the anionic redox reversibility with suppressed irreversible oxygen release but also alleviate the interlayer slipping induced by anionic redox and reinforce the TM–O framework with inhibited undesired P2-Z phase transition at high voltages. This effectively preserves the robust Na$^+$ diffusion channels and prevents the formation of microcracks caused by excessive interlayer slipping, thereby minimizing the surface side reactions (Fig. 1b). Because of these advantages, NLMRO delivers improved electrochemical performance with a reversible anionic redox reaction and superior long-term cycling stability. This work provides a facile avenue to strengthen π-type interaction for developing high-performance layered oxide cathodes for SIBs.

Results and discussion

Stabilizing the anionic redox reaction critically depends on the strength of the π-type interaction between TM and oxygen atoms, as this dictates the extent of the stabilizing splitting between π/π* orbitals. According to ligand field theory, the strength of this π-type interaction is largely determined by the energy level alignment between the TM t_{2g} orbitals and O 2p orbitals.[26] Among various TM elements, Ru emerges as a promising candidate to enhance the π-type interaction with oxygen because its 4d orbitals are inherently more delocalized compared with the 3d orbitals of first-row TMs (e.g., Mn),[27] promoting better orbital overlap with oxygen. Additionally, the electronegativity of Ru (2.20) is larger than that of Mn (1.55), which suggests a stronger electronic interaction with oxygen. Furthermore, the shorter Ru–O bond length (1.882 Å) compared to the Mn–O bond (1.894 Å) contributes to a larger crystal field splitting (Δ_o). This results in a lower-lying t_{2g} energy level for Ru, which in turn promotes the formation of π* orbitals with more dominant oxygen character, thereby leading to stronger π-type interaction stabilizing the anionic redox process (Fig. S1 and Table S1†). Therefore, Ru was chosen to substitute Mn in NLMO, specifically to strengthen the inherently weak π-type interaction, aiming to enhance the anionic redox reversibility and stability (Fig. 1c and S2†).

NLMO and NLMRO were synthesized using a conventional solid-solution method. X-ray diffraction (XRD) was utilized to characterize the crystal structure. As shown in Fig. S3,† both NLMO and NLMRO exhibit a pure P2-type phase with all diffraction peaks indexed to the $P6_3/mmc$ space group. For NLMO, however, several weak diffraction peaks are observed in the 20–30° range (Fig. S4†), which are characteristic of a ribbon-like superstructure arising from the in-plane ordering of Li$^+$ and Mn^{4+}. It is worth noting that the (002) peak of NLMRO shifts to lower angles compared to that of NLMO, indicating an expansion of the c axis. Rietveld refinement results (Fig. 2a, b and Tables S2 and S3†) show that the c axis increases from 11.11 Å for NLMO to 11.16 Å for NLMRO. Additionally, it is very likely that the strong covalent interaction between Ru and O compresses the RuO$_6$ octahedra within the TMO$_2$ layers, resulting in increased Na-layer spacing in NLMRO (3.87 Å)

compared to NLMO (3.71 Å). This expanded interlayer spacing is expected to enhance the Na$^+$ diffusion kinetics during electrochemical cycling.

The oxidation states of TM elements in NLMO and NLMRO were investigated using synchrotron-based X-ray absorption near-edge structure (XANES) spectroscopy. The Mn K-edge XANES spectra of NLMO and NLMRO show an average Mn valence state of approximately +4 (Fig. 2c), suggesting that the introduction of Ru has negligible influence on the electronic structure of Mn. In contrast, the position of Ru K-edge XANES absorption edge of NLMRO is very close to that of RuO$_2$, suggesting that Ru exists predominantly in the +4 oxidation state (Fig. 2d).[28,29] To quantitatively analyze the local atomic structures of NLMRO, Fourier transform of extended X-ray absorption fine structure (FT-EXAFS) spectra of Mn and Ru in R-space were fitted using the least-squares method. The results (Fig. 2e and f) demonstrate that both Mn and Ru in NLMRO have a first-shell coordination number of 6, confirming that the introduced Ru atoms mainly occupy the octahedral sites within the TMO$_6$ framework (Fig. 2g).

Scanning electron microscopy (SEM) and high-resolution transmission electron microscopy (HRTEM) were further employed to examine the morphological and crystallographic characteristics of NLMO and NLMRO. As shown in Fig. S5,† both samples possess regular hexagonal plate-like morphologies with a particle size ranging from 2.0 to 3.0 μm. Notably, the (002) lattice fringe distance slightly increases from 0.539 nm for NLMO to 0.567 nm for NLMRO (Fig. 2h and S6†), which is in good agreement with the expansion of the c axis observed in XRD results. Moreover, energy dispersive spectroscopy (EDS) mappings reveal the uniform distribution of all elements throughout NLMRO (Fig. 2i). Collectively, these results provide unequivocal evidence of the successful incorporation of Ru into NLMRO, resulting in expanded interlayer spacing and enhanced π-type interaction within the crystal structure.

The electrochemical properties of NLMO and NLMRO were systematically evaluated using Na half cells within a voltage range of 2.0–4.5 V to explore the impact of enhanced π-type interaction. The galvanostatic charge/discharge profiles of NLMO and NLMRO at a current rate of 0.2 C (1.0 C = 170.0 mAh g^{-1}) are shown in Fig. 3a. NLMO exhibits a distinct charge plateau in the high-voltage region, which corresponds to the anionic redox reaction. In contrast, NLMRO displays a sloping region below 4.0 V followed by the anionic redox plateau, which should be related to the oxidation of Ru^{4+} to Ru^{5+}.[26] During discharge, NLMRO exhibits a smooth slope, which corresponds to the reduction of O, Ru, and Mn, delivering a higher discharge capacity of 153.4 mAh g^{-1} compared to that of NLMO (97.7 mAh g^{-1}). The enhanced capacity can be attributed to the combination of extra contribution from Ru^{4+}/Ru^{5+} redox and stabilized anionic redox.

Cyclic voltammetry (CV) characterization further reveals that the oxidation peak for NLMRO above 4.0 V is considerably broadened with strengthened π-type interaction (Fig. 3b). To scrutinize the specific redox processes contributing to this widened oxidation peak, dQ/dV plots at varying cut-off voltage windows were constructed (Fig. 3c). The dQ/dV plot at the cut-
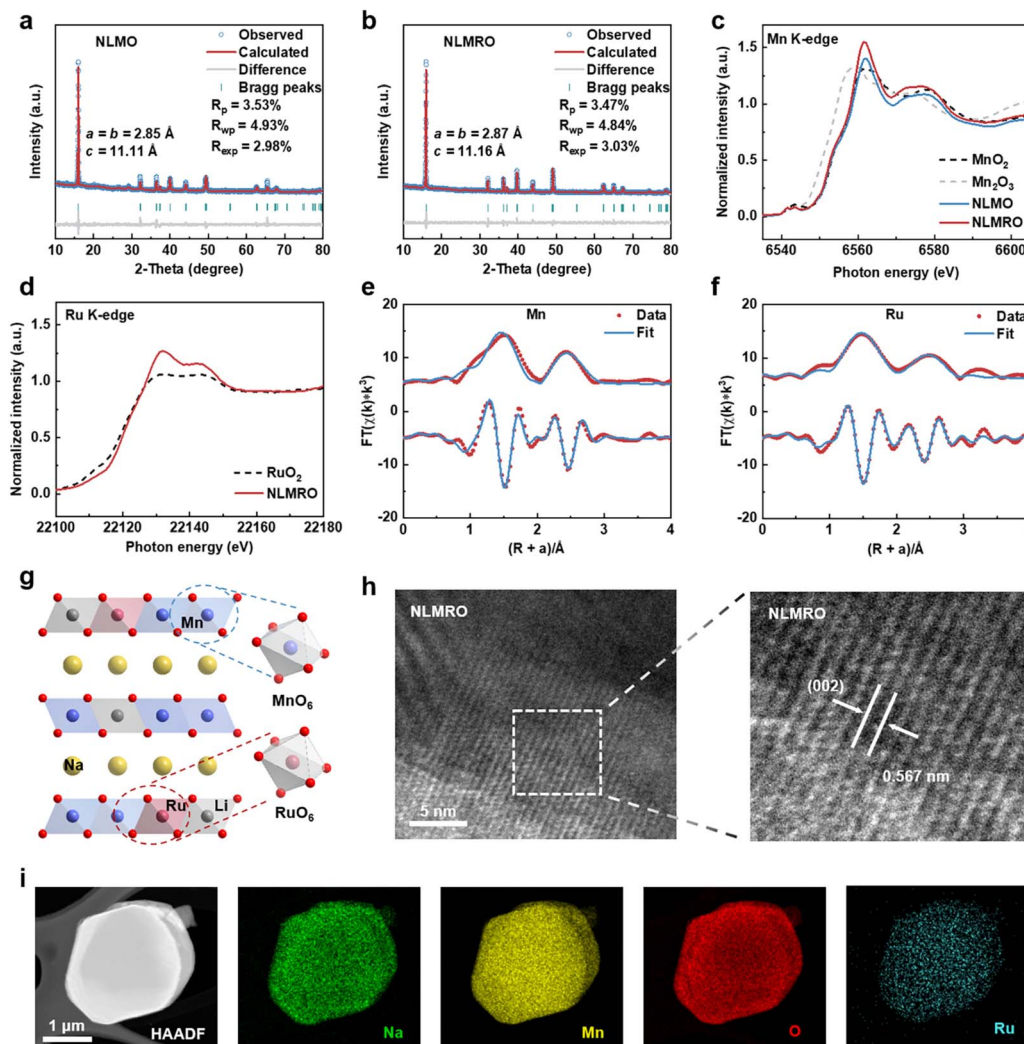
Fig. 2 Structural characterization of NLMO and NLMRO. XRD patterns and the corresponding Rietveld refinements of (a) NLMO and (b) NLMRO. (c) Mn K-edge XANES spectra of NLMO and NLMRO. (d) Ru K-edge XANES spectra of NLMRO. Least-square fits of the calculated FT-EXAFS phase and amplitude functions to the experimental (e) Mn and (f) Ru K-edge EXAFS spectra of NLMRO. (g) Proposed crystal structure of NLMRO. (h) TEM images of NLMRO. (i) Elemental mappings of NLMRO.

off voltage of 4.3 V demonstrates one peak at 4.1 V corresponding to Ru redox activity,[17] while the additional peak at 4.45 V is observed when the cut-off voltage is increased to 4.5 V, which can be attributed to the oxidation of oxygen.[26] Benefiting synergistically from the introduced Ru^{4+}/Ru^{5+} redox couple and more stabilized anionic redox facilitated by strengthened π-type interaction, NLMRO exhibits a drastically increased specific capacity with remarkable capacity retention after 100 cycles compared to NLMO (Fig. 3d).

Furthermore, galvanostatic intermittent titration technique (GITT) measurements were conducted to determine the Na+ diffusion coefficients (D_{Na+}). As shown in Fig. S7,† the D_{Na+} values of NLMO experience a substantial decrease at high voltages due to the sluggish anionic redox, while the D_{Na+} values of NLMRO remain within the range of 10^{-9}–10^{-10} cm² s^{-1} throughout the entire voltage window, suggesting the enhanced anionic redox kinetics because of strengthened π-type

interaction.[30] In addition, electrochemical impedance spectroscopy (EIS) results reveal much lower charge transfer resistance for NLMRO (Fig. 3e), indicating that the incorporation of Ru could reduce the electron transfer resistance. As a consequence, the rate performance of NLMRO is largely improved, with the discharge capacities of 150.8, 104.7, 101.6, 86.7, and 68.5 mAh g^{-1} at the current densities of 0.2, 0.5, 1.0, 2.0, and 5.0 C, respectively, all of which are superior to those of NLMO (Fig. 3f). Moreover, NLMRO demonstrates largely improved cycling stability at a high current density of 1.0 C with a capacity retention of 81.2% after 200 cycles, while a capacity retention of mere 45.5% is achieved for NLMO (Fig. 3g), suggesting the improved structural stability over cycling for the former.

Therefore, *in situ* XRD experiments were conducted to investigate the structural evolution over cycling. For NLMO, the intensity of the (002) peak undergoes significant fluctuations in the high-voltage region accompanied by the appearance of
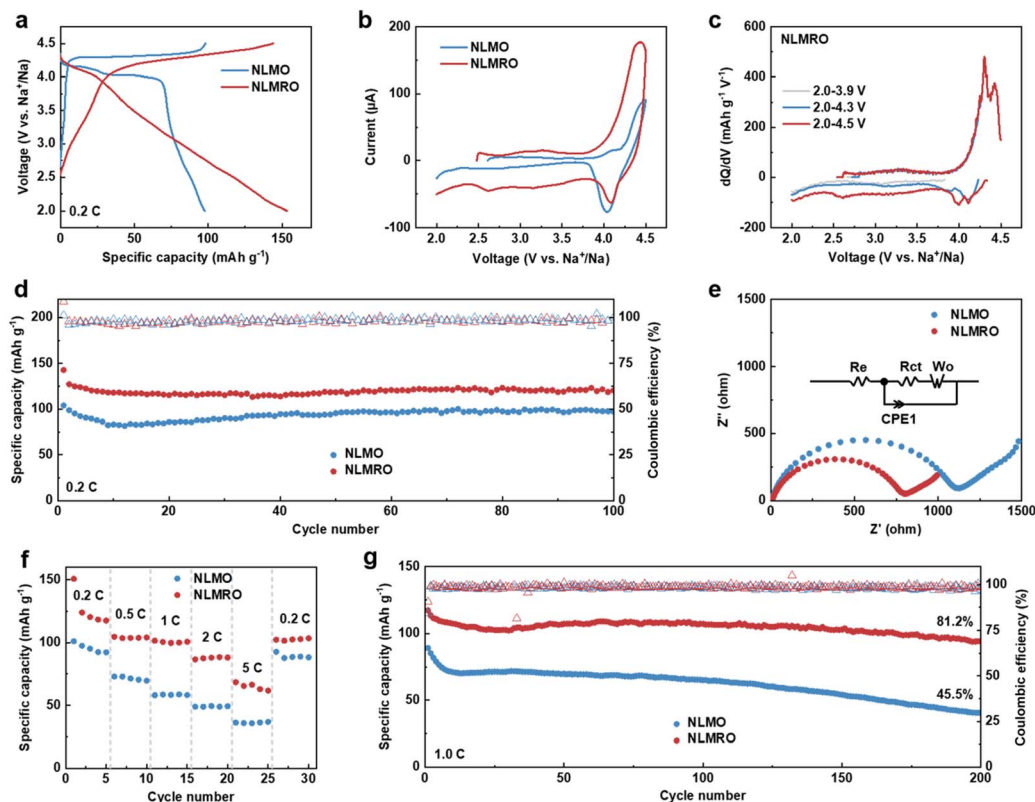
Fig. 3 Electrochemical characterization of NLMO and NLMRO. (a) Voltage profiles of NLMO and NLMRO at 0.2 C during the first cycle. (b) CV curves of NLMO and NLMRO during the first cycle. (c) dQ/dV curves of NLMRO at different cut–off voltage windows. (d) Cycling performance of NLMO and NLMRO at 0.2 C. (e) EIS curves of NLMO and NLMRO. (f) Rate performance of NLMO and NLMRO. (g) Cycling performance of NLMO and NLMRO at 1.0 C.

a new diffraction peak at 16.7° (Fig. 4a and c), corresponding to the formation of the Z phase that is an O/P intergrowth structure positioned between pure P and O phases.[19,31] The formation of this O-type stacking component, along with the degradation of P2-type slab integrity, implies severe interlayer slippage caused by variations in the TM–O bonds during the aggressive anionic redox reaction. Moreover, the P2-Z phase transition is invariably accompanied by significant lattice distortion and substantial volume change, which lead to inferior electrochemical kinetics and diminished performance over extended cycles.[32] In contrast, for NLMRO, the intensity of the (002) peak only exhibits slight changes without the appearance of new peaks (Fig. 4b and c), implying a pure solid-solution reaction throughout the entire electrochemical process. This suppressed phase transition should be closely related to the enhanced π-type interaction, which could suppress the drastic TM–O bond variations that is typically caused by oxygen oxidation/release at high voltage,[33] leading to enhanced structural integrity over cycling.

To quantitatively understand the evolution of lattice parameters, *in situ* XRD patterns of NLMRO were refined (Fig. 4d). Upon charging, the a/b lattice parameters decrease as a result of Ru oxidation. Concurrently, the c lattice parameter exhibits a two-stage behavior: it initially increases in the low voltage region owing to Na$^+$ extraction, which enhances the

O^{2-}–O^{2-} electrostatic repulsion and expands the interlayer spacing; in the high voltage region, it unexpectedly decreases, reflecting a negative lattice expansion tendency.[34] This unusual phenomenon could be attributed to the sequential TM and O oxidation processes: the oxidation of high-electronegativity Ru in the initial stage leads to the increase of interlayer electrostatic repulsion and thus expanded interlayer spacing, while the further anionic redox reaction within the π-type network in the high voltage region lowers the electron density around O atoms, ultimately affecting the interlayer interactions and contributing to the observed lattice parameter contraction. Therefore, NLMRO exhibits a remarkably small volume change of only 1.0% over the entire charge/discharge process. Overall, NLMRO undergoes a complete solid-solution reaction with minimal volume change, providing robust structural integrity for enhanced charge transfer kinetics and cycling stability upon cycling (Fig. 4e).[35]

It should be mentioned that the Z phase contains neighboring O-type stacking arrangements at high states of charge, which could induce severe slippage along the a/b axis.[32] This slippage usually results in the formation of cracks at the surface that unfortunately promote detrimental side reactions with the electrolyte.[36] TEM images of both NLMO and NLMRO after 10 cycles were collected (Fig. 5a and b). Noticeable surface cracks are observed on NLMO, indicating structural collapse due to P2-
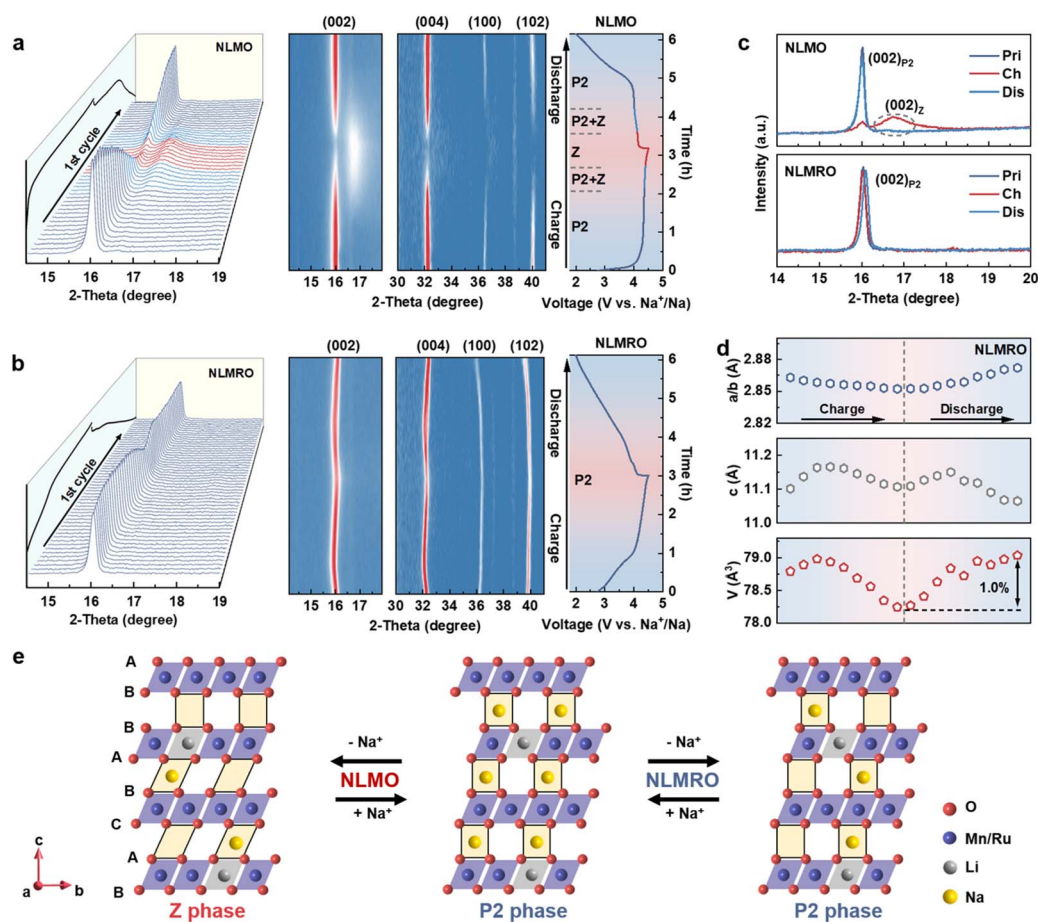
Fig. 4 Structure evolution of NLMO and NLMRO. *In situ* XRD patterns of (a) NLMO and (b) NLMRO during the first cycle at 0.2 C. (c) *In situ* XRD patterns of the (002) peak of NLMO and NLMRO in different states of charge. (d) Variation of unit cell parameters a/b, c and V for NLMRO. (e) Schematic illustration of the phase transition processes of NLMO and NLMRO.

Z phase transition. In sharp contrast, NLMRO remains unchanged throughout the bulk and surface, demonstrating superior structural stability during cycling. To further understand the surface stability of NLMO and NLMRO, O K-edge XANES spectra in different states of charge were measured. For NLMO, an obvious peak at 534.0 eV attributed to CO_3^{2-} species is observed in the fully discharged state (Fig. 5c), indicating severe electrolyte decomposition and detrimental interfacial reactions for NLMO.[13] In contrast, because of the suppressed interfacial side reaction, no CO_3^{2-} species can be observed for NLMRO (Fig. 5d). Furthermore, *in situ* differential electrochemical mass spectrometry (DMES) results indicate that a prominent O_2 peak appears at high charge voltages for NLMO, suggesting that the inherently weaker π-type interaction in NLMO is insufficient to stabilize oxidized oxygen species and thereby leads to inevitable oxygen release (Fig. 5e). Conversely, no such oxygen release is observed for NLMRO (Fig. 5f), confirming that the introduction of Ru can not only suppress the harmful phase transition but also strengthen the π-type interaction to stabilize oxygen during the anionic redox reaction.

Therefore, the anionic redox reaction was investigated using the mapping of resonant inelastic X-ray scattering (mRIXS),

a powerful tool for scrutinizing the oxidized oxygen states in battery cathodes.[37,38] The broad features at ~525 eV emission energy observed in all measured samples originate from the TM–O hybridized states that split into t_{2g} and e_g states (Fig. 5g–i).[39,40] Notably, the oxidized oxygen fingerprint feature at 531.0 eV excitation energy and 523.7 eV emission energy emerges upon charging and disappears in the following discharge for NLMRO. A similar phenomenon is also observed in the second cycle (Fig. 5i), suggesting the reversible anionic redox reaction.[41] The intensity change of oxidized oxygen feature is further highlighted in the individual RIXS spectra extracted from the mRIXS results at resonant and off-resonant excitation energies (Fig. 5j–l),[42] providing compelling evidence for the stabilized and reversible anionic redox behavior facilitated by the enhanced π-type interaction. To further probe the nature of these oxidized oxygen species and investigate whether trapped bulk O_2 is formed, *ex situ* Raman spectroscopy was conducted. As shown in Fig. S8,† NLMO exhibits a distinct new peak at ~474 cm^{-1} after charging, which can be attributed to the vibrational mode of Mn–(O–O) species that is a hallmark of trapped molecular O_2 within the lattice.[43] The intensity of this peak increases after further cycling, indicating a progressive
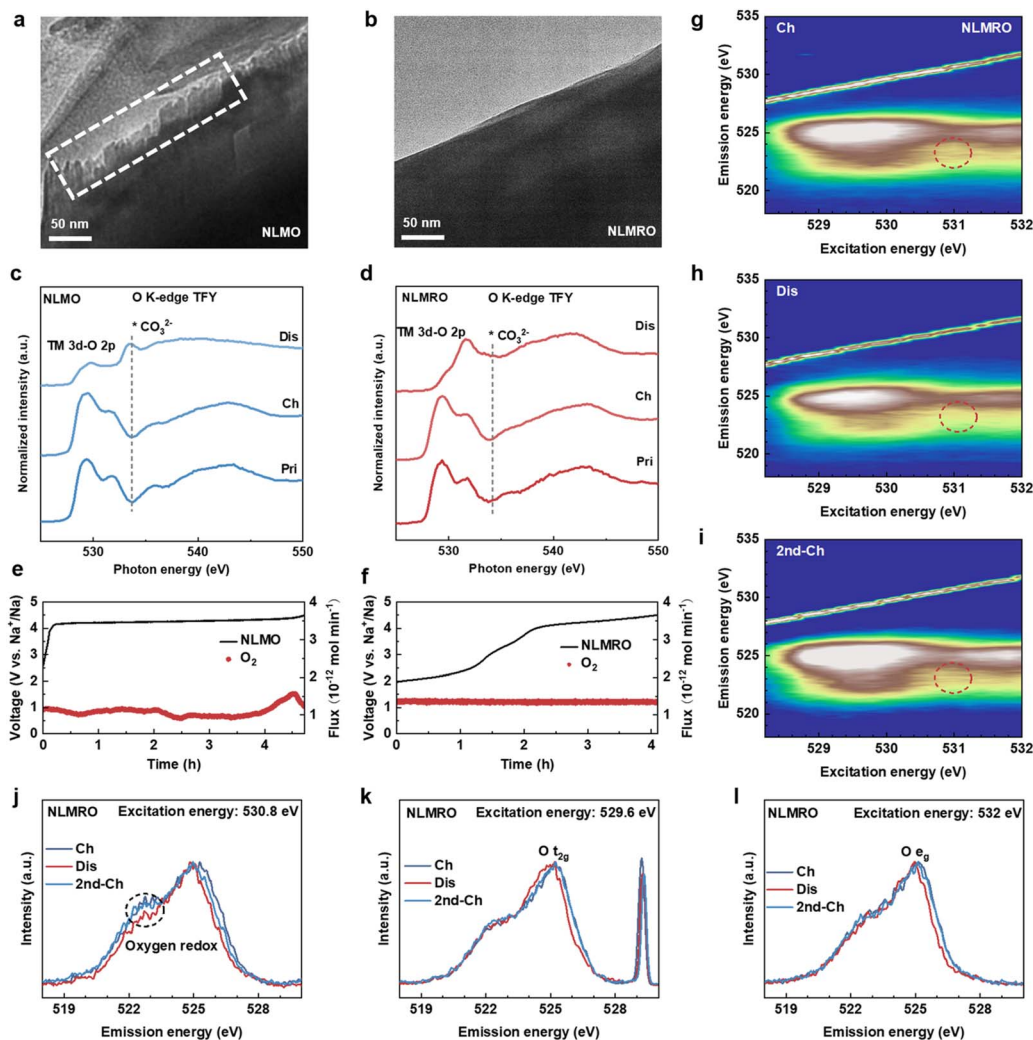
Fig. 5 TEM images of (a) NLMO and (b) NLMRO after 10 cycles. O K-edge XANES spectra of (c) NLMO and (d) NLMRO in different states of charge. *In situ* DEMS results of (e) NLMO and (f) NLMRO. (g–i) O K-edge mRIXS of NLMRO in different states of charge. The cycles highlight the oxidized lattice oxygen feature. RIXS spectra of NLMRO in different states of charge with excitation energies of (j) 530.8 eV, (k) 529.6 eV, and (l) 532.0 eV.

structural degradation that facilitates O_2 trapping. In stark contrast, no such peak is observed for NLMRO in the same states of charge, implying that the formation of trapped bulk O_2 is effectively suppressed. Overall, the oxidized oxygen induced by highly active non-bonding O 2p orbitals has been effectively stabilized by the strong π-type interaction with Ru in NLMRO, leading to effective inhibition of oxygen release and remarkable reversibility of anionic redox during cycling.

To further unravel the charge compensation mechanism of improved NLMRO electrochemistry, XANES was employed to investigate the electronic structure evolution of Ru and Mn. Fig. 6a shows the Ru L_3-edge XANES spectra in different states of charge (Fig. 6b), which directly probe the unoccupied 4d states *via* dipole-allowed 2p-4d transitions. Two prominent peaks are observed for the spectrum of pristine NLMRO, corresponding to the t_{2g} and e_g states, respectively.[44] Upon charging, the absorption peaks gradually shift toward higher energy until 4.3 V with the oxidation state to +5, further demonstrating the

establishment of a $t_{2g}^3 e_g^0$ electronic configuration for Ru prior to oxygen oxidation for the construction of strengthened π-type interaction. In the following discharge process, the absorption peaks shift back to the original position, suggesting the high reversibility of the Ru^{4+}/Ru^{5+} redox reaction, as also confirmed by Ru K-edge XANES results (Fig. 6c). Furthermore, the high reversibility is also retained after 10 cycles (Fig. S9†), which ensures continuous stabilization of the oxygen redox reaction throughout extended cycles.

While the reversible Ru redox is important for dynamically strengthening π-type interaction to achieve reversible anionic redox, the resulting stability of oxygen, in turn, could considerably impact the valence state of TM, especially for the region near the surface, considering the interfacial side reactions.[45] Therefore, Mn L-edge XANES spectra in inverse partial fluorescence yield (iPFY) mode were collected for NLMO and NLMRO in different states of charge to avoid the self-absorption effect (Fig. 6d and e),[13] which were also fitted using a linear
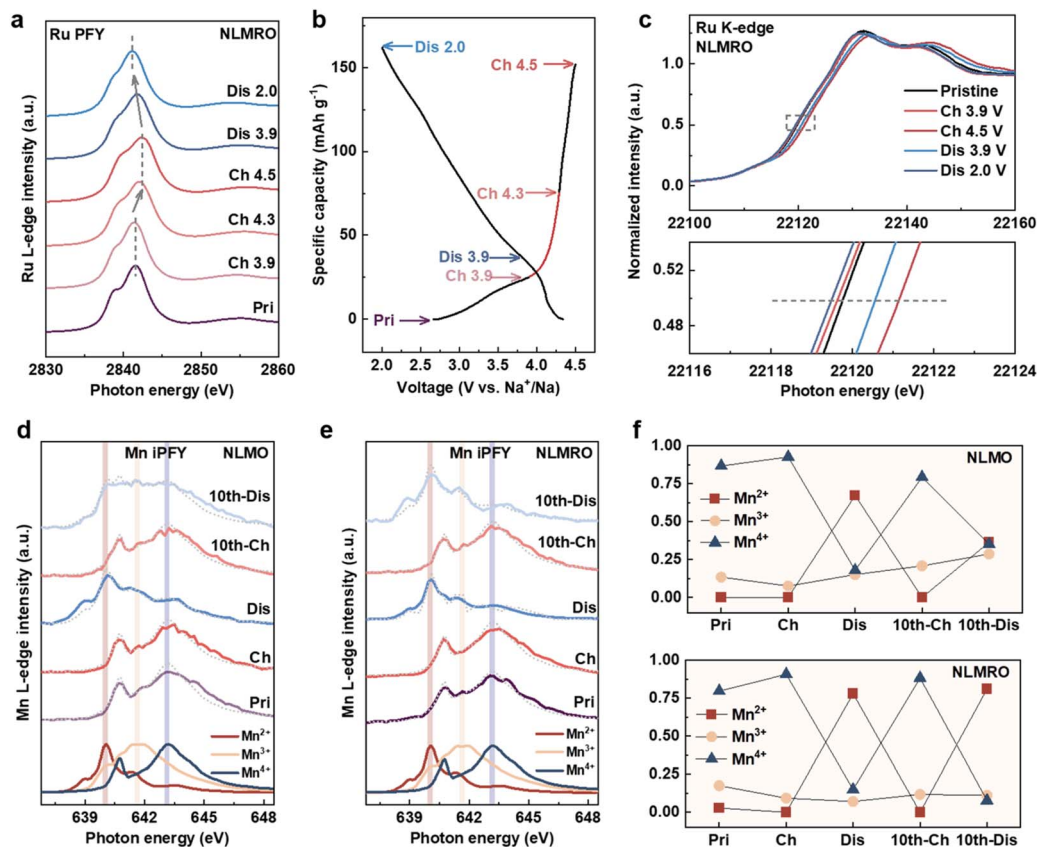
Fig. 6 Charge compensation mechanism of NLMO and NLMRO. (a) Ru L$_3$-edge XANES spectra of NLMRO in different states of charge. (b) Charge/discharge voltage profiles of the first cycle for NLMRO. The points measured by XANES spectra are marked with arrows. (c) Ru K-edge XANES spectra in different states of charge for NLMRO. (d–f) Mn L-edge XANES spectra and quantitative fitting results of NLMO and NLMRO in different states of charge.

combination of Mn^{2+}/Mn^{3+}/Mn^{4+} reference spectra to quantitatively analyze the evolution of Mn valence states in different states of charge (Tables S4 and S5†).[46,47] The fitting results (dotted lines) show good agreement with the experimental data (solid lines), guaranteeing the reliability of the quantitative Mn valence states. The Mn valence state of NLMRO is similar to that of NLMO in the pristine state, in good agreement with the Mn K-edge XANES spectra. Notably, no apparent change is observed for both samples owing to the dominant Mn^{4+} upon charging (Fig. 6f). In the fully discharged state, the Mn^{2+} content increases to 67.13% for NLMO and 77.94% for NLMRO because of the redox conversion from Mn^{4+} to Mn^{2+} on the cathode surface. Notably, the Mn^{4+} content decreases to 79.22% in the charged state, while the Mn^{2+} content decreases to mere 36.27% in the discharged state for NLMO after 10 cycles, which are primarily induced by the irreversible oxygen release and subsequent surface cracking induced side reactions and Mn dissolution into the electrolyte.[48] In contrast, NLMRO delivers a remarkable Mn^{2+}/Mn^{4+} redox reversibility after 10 cycles, which is a direct consequence of the stabilized oxygen environment achieved through the dynamically modulated anionic redox via enhanced Ru–O π-type interaction. By effectively preventing irreversible oxygen loss and maintaining structural

integrity, the local coordination around Mn is well preserved and Mn dissolution is minimized.

Additionally, the Mn K-edge XANES spectra reveal that the absorption edge of NLMRO shifts to a lower energy position compared to that of NLMO in the fully discharged state (Fig. 7a and b), indicating a more pronounced reduction of Mn, consistent with the Mn L-edge iPFY spectra. It is worth mentioning that the good reversibility and cyclability of TM redox arising from reversible anionic redox have tremendous effects on the stability of TMO$_6$ octahedra. Notably, the pre-edge features, which contain the information on TMO$_6$ octahedral symmetry,[49] also show differences between NLMO and NLMRO (Fig. 7c). The pre-edge feature of NLMO intensifies in the charged state, which can be ascribed to serious TMO$_6$ octahedra distortion induced by highly active anionic redox occurring in the high voltage region, consistent with the P2-Z phase transition observed in the in situ XRD results. In contrast, the pre-edge feature intensity of NLMRO remains almost constant between the pristine and charged states, indicating that the strengthened π-type interaction successfully mitigates the TM–O bond variations associated with anionic redox, thereby preserving the TMO$_6$ octahedral symmetry and preventing severe distortion during the charge process.
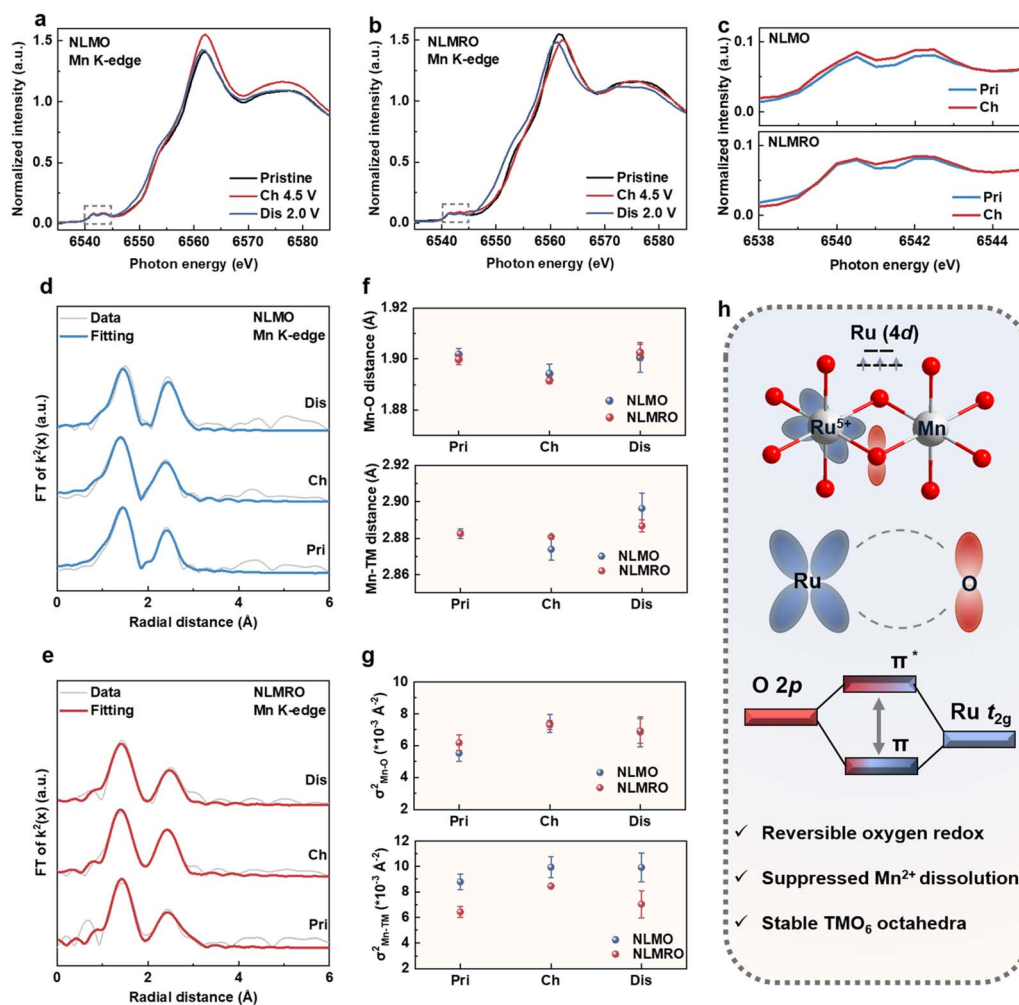
Fig. 7 Local structural characterization of NLMO and NLMRO. Mn K-edge XANES spectra in different states of charge for (a) NLMO and (b) NLMRO. (c) Enlarged view of the marked areas in (a and b). Mn K-edge FT-EXAFS spectra of (d) NLMO and (e) NLMRO in different states of charge. (f) Bond distances and (g) Debye–Waller factors σ^2 of Mn–O and Mn–TM coordination shells of NLMO and NLMRO. (h) Schematic illustration of the role of π-type interaction in NLMRO.

To further understand the evolution of TMO$_6$ octahedra in both samples, Mn K-edge FT-EXAFS spectra were fitted in R-space and K-space to obtain quantitative information about the local coordination environment changes during cycling (Tables S6 and S7†). The fitting curves are in good agreement with the experimental data (Fig. 7d, e, S10 and S11†), showing that the achieved quantitative data are reliable. For both NLMO and NLMRO, the Mn–O bond distance decreases during the charging process (Fig. 7f). Given that Mn predominantly maintains a +4 oxidation state in both pristine materials, this bond length contraction during charge is primarily attributed to changes associated with anionic redox activity. During the subsequent discharge process, the Mn–O bond distance increases as expected because of the reduction of Mn and O species. For NLMO, it changes from 1.894 Å to 1.901 Å, while it increases considerably from 1.885 Å to 1.902 Å for NLMRO. The larger reversible change in NLMRO is consistent with the more complete and reversible Mn reduction observed in the Mn K-edge XANES results, likely facilitated by the reversible anionic

redox. Notably, the Mn–TM bond distance exhibits trends similar to those of the Mn–O bond distance, which is expected for the edge-shared octahedral structures where the TM–O bond changes could influence the TM–TM bond. More specifically, NLMO shows a relatively large and less reversible change for the Mn–TM bond distance upon discharge. This could be influenced by Mn redox and irreversible structural evolution, such as Li migration into the Na layers, which might be facilitated by the P2-Z phase transition.[50] In contrast, NLMRO displays a more moderate and reversible evolution for the Mn–TM bond distance over cycling. This suggests that the suppressed P2-Z phase transition in NLMRO owing to strengthened π-type interaction could maintain a more stable framework to potentially hinder the detrimental Li migration[51] and contribute to the preservation of local TM arrangement.

The contour plots of Mn K-edge wavelet-transformed EXAFS spectra were utilized to get a visualized evolution of TMO$_6$ octahedra during cycling (Fig. S12†). It is evident that the scattering peak attributed to the Mn–O shell shows inconsistent

intensity between the pristine and fully discharged states in NLMO, indicating irreversible evolution of the Mn–O coordination environment. To further quantify this structural evolution, the Debye–Waller factors (σ^2), which are associated with the structural disorder, were analyzed for both samples (Fig. 7g).[52] The σ^2 value of Mn–O coordination increases from 5.52×10^{-3} to 7.38×10^{-3} for NLMO, whereas it increases more moderately from 6.18×10^{-3} to 7.30×10^{-3} for NLMRO during the charging process, demonstrating better preservation of the local Mn–O coordination environment for the latter, considering the regulated anionic redox by strengthened π-type interaction. In contrast, for the Mn–TM coordination of NLMO, the σ^2 value increases from 8.79×10^{-3} to 9.94×10^{-3} during the charging process but fails to recover to the initial value upon discharge (9.92×10^{-3}), which possibly results from permanent distortion within the bulk structure induced by oxygen loss and subsequent local TM rearrangement and/or defect formation.[13,52] In sharp contrast, NLMRO displays a highly reversible σ^2 evolution for the Mn–TM coordination as a consequence of the reversible anionic redox and preserved rigidity of TMO_6 octahedra.

Based on the above analysis, we can unambiguously elucidate the origin of improved structural stability and anionic redox behavior for NLMRO, as illustrated in Fig. 7h. The sequential oxidation of Ru and O ensures that the Ru^{5+} with a $4d^3$ electronic configuration appears before the anionic redox begins, resulting in strong π-type interaction between Ru t_{2g} orbitals and orphaned O 2p states within the Na–O–Li configuration. The splitting of π-type bonding/anti-bonding orbitals could stabilize the oxidized oxygen species after the anionic redox takes place, effectively inhibiting irreversible oxygen release and achieving reversible anionic redox reaction. Concurrently, the stabilized anionic redox reaction could also suppress the phase transition in the high voltage region and mitigate the interfacial side reactions with limited TM dissolution, leading to stable TMO_6 octahedra throughout the electrochemical process. As a consequence, remarkable structural stability from the bulk to surface and superior electrochemical performance are achieved for NLMRO over extended cycles.

Conclusions

In summary, this work demonstrates an effective strategy of strengthening TM–O π-type interaction to achieve highly reversible anionic redox and superior structural stability by introducing a reversible Ru^{4+}/Ru^{5+} redox couple in P2-type layered oxide cathodes. We show that the half-filled t_{2g} orbitals of Ru^{5+} formed before the onset of anionic redox establish strengthened π-type interaction with non-bonding O 2p orbitals within the Na–O–Li configuration, which effectively stabilizes oxidized oxygen and suppresses irreversible oxygen release accompanied by a complete solid-solution behavior with inhibited P2-Z phase transition over cycling. This robust structural integrity, from the bulk to surface, in turn prevents Mn dissolution and preserves TMO_6 octahedral stability. As a consequence, the resulting NLMRO exhibits enhanced specific capacity, rate performance, and long-term cycling

stability. This study underscores the critical role of the TM–O π-type interaction in stabilizing anionic redox and enhancing structural integrity, offering practical guidance for the rational design of high-performance layered oxide cathodes for SIBs.

Data availability

The data supporting this article have been included as part of the ESI.†

Author contributions

Zheng Zhou: investigation, data curation, visualization, writing of the original draft, manuscript review and editing. Chen Cheng: investigation, writing of the original draft. Shuyuan Chen: data curation, visualization. Tong Chen: data curation, visualization. Lei Wang: data curation. Tianran Yan: data curation. Weidong Xu: data curation, visualization. Shiqi Shen: data curation. Jianrong Zeng: data curation, supervision. Liang Zhang: investigation, supervision, writing of the original draft, manuscript review and editing.

Conflicts of interest

There are no conflicts to declare.

Acknowledgements

References

1 H. Ren, Y. Li, Q. Ni, Y. Bai, H. Zhao and C. Wu, Unraveling Anionic Redox for Sodium Layered Oxide Cathodes: Breakthroughs and Perspectives, *Adv. Mater.*, 2022, **34**, 2106171.

2 R. A. House, G. J. Rees, K. McColl, J.-J. Marie, M. Garcia-Fernandez, A. Nag, K.-J. Zhou, S. Cassidy, B. J. Morgan, M. Saiful Islam and P. G. Bruce, Delocalized Electron Holes on Oxygen in a Battery Cathode, *Nat. Energy*, 2023, **8**, 351–360.

3 Y.-J. Park and D.-H. Seo, Capturing the Hole States of Oxygen, *Nat. Energy*, 2023, **8**, 323–324.

4 A. Gao, Q. Zhang, X. Li, T. Shang, Z. Tang, X. Lu, Y. Luo, J. Ding, W. H. Kan, H. Chen, W. Yin, X. Wang, D. Xiao, D. Su, H. Li, X. Rong, X. Yu, Q. Yu, F. Meng, C. Nan, C. Delmas, L. Chen, Y.-S. Hu and L. Gu, Topologically Protected Oxygen Redox in a Layered Manganese Oxide

Cathode for Sustainable Batteries, *Nat. Sustainability*, 2022, **5**, 214–224.

5 X. Cai, Z. Shadike, N. Wang, L. Liu, E. Hu and J. Zhang, Oxygen Redox Chemistry: A New Approach to High Energy Density World, *Next Mater.*, 2024, **2**, 100086.

6 R. A. House, U. Maitra, M. A. Pérez-Osorio, J. G. Lozano, L. Jin, J. W. Somerville, L. C. Duda, A. Nag, A. Walters, K.-J. Zhou, M. R. Roberts and P. G. Bruce, Superstructure Control of First-Cycle Voltage Hysteresis in Oxygen-Redox Cathodes, *Nature*, 2019, **577**, 502–508.

7 C. Ma, J. Alvarado, J. Xu, R. J. Clément, M. Kodur, W. Tong, C. P. Grey and Y. S. Meng, Exploring Oxygen Activity in the High Energy P2-Type $Na_{0.78}Ni_{0.23}Mn_{0.69}O_2$ Cathode Material for Na-Ion Batteries, *J. Am. Chem. Soc.*, 2017, **139**, 4835–4845.

8 E. Boivin, R. A. House, M. A. Pérez-Osorio, J.-J. Marie, U. Maitra, G. J. Rees and P. G. Bruce, Bulk O_2 Formation and Mg Displacement Explain O-Redox in $Na_{0.67}Mn_{0.72}Mg_{0.28}O_2$, *Joule*, 2021, **5**, 1267–1280.

9 D.-H. Seo, J. Lee, A. Urban, R. Malik, S. Kang and G. Ceder, The Structural and Chemical Origin of the Oxygen Redox Activity in Layered and Cation-Disordered Li-Excess Cathode Materials, *Nat. Chem.*, 2016, **8**, 692–697.

10 U. Maitra, R. A. House, J. W. Somerville, N. Tapia-Ruiz, J. G. Lozano, N. Guerrini, R. Hao, K. Luo, L. Jin, M. A. Pérez-Osorio, F. Massel, D. M. Pickup, S. Ramos, X. Lu, D. E. McNally, A. V. Chadwick, F. Giustino, T. Schmitt, L. C. Duda, M. R. Roberts and P. G. Bruce, Oxygen Redox Chemistry without Excess Alkali-Metal Ions in $Na_{2/3}[Mg_{0.28}Mn_{0.72}]O_2$, *Nat. Chem.*, 2018, **10**, 288–295.

11 W. E. Gent, K. Lim, Y. Liang, Q. Li, T. Barnes, S.-J. Ahn, K. H. Stone, M. McIntire, J. Hong, J. H. Song, Y. Li, A. Mehta, S. Ermon, T. Tyliszczak, D. Kilcoyne, D. Vine, J.-H. Park, S.-K. Doo, M. F. Toney, W. Yang, D. Prendergast and W. C. Chueh, Coupling between Oxygen Redox and Cation Migration Explains Unusual Electrochemistry in Lithium-Rich Layered Oxides, *Nat. Commun.*, 2017, **8**, 2091.

12 K. Luo, M. R. Roberts, R. Hao, N. Guerrini, D. M. Pickup, Y.-S. Liu, K. Edström, J. Guo, A. V. Chadwick, L. C. Duda and P. G. Bruce, Charge-Compensation in 3d-Transition-Metal-Oxide Intercalation Cathodes through the Generation of Localized Electron Holes on Oxygen, *Nat. Chem.*, 2016, **8**, 684–691.

13 C. Cheng, Z. Zhuo, X. Xia, T. Liu, Y. Shen, C. Yuan, P. Zeng, D. Cao, Y. Zou, J. Guo and L. Zhang, Stabilized Oxygen Vacancy Chemistry toward High-Performance Layered Oxide Cathodes for Sodium-Ion Batteries, *ACS Nano*, 2024, **18**, 35052–35065.

14 A. Konarov, H. J. Kim, J.-H. Jo, N. Voronina, Y. Lee, Z. Bakenov, J. Kim and S.-T. Myung, High-Voltage Oxygen-Redox-Based Cathode for Rechargeable Sodium-Ion Batteries, *Adv. Energy Mater.*, 2020, **10**, 2001111.

15 S. Chen, C. Cheng, X. Xia, L. Wang, T. Chen, Y. Shen, X. Zhou, W. Xv, Z. Zhou, P. Zeng and L. Zhang, Reversible Oxygen Redox with Enhanced Structural Stability Through Covalency Modulation for Layered Oxide Cathodes, *Small*, 2024, **20**, 2406542.

16 X. Zhou, T. Liu, C. Cheng, X. Xia, Y. Shen, L. Wang, Y. Xie, B. Wang, Y. Zou, D. Cao, Y. Su and L. Zhang, Achieving Complete Solid-Solution Reaction in Layered Cathodes with Reversible Oxygen Redox for High-Stable Sodium-Ion Batteries, *Energy Storage Mater.*, 2025, **74**, 103895.

17 B. Li, R. Shao, H. Yan, L. An, B. Zhang, H. Wei, J. Ma, D. Xia and X. Han, Understanding the Stability for Li-Rich Layered Oxide Li_2RuO_3 Cathode, *Adv. Funct. Mater.*, 2016, **26**, 1330–1337.

18 Z. Zhang, H. Zhang, Y. Wu, W. Yan, J. Zhang, Y. Zheng and L. Qian, Advances in Doping Strategies for Sodium Transition Metal Oxides Cathodes: A Review, *Front. Energy*, 2024, **18**, 141–159.

19 D. Eum, B. Kim, J.-H. Song, H. Park, H.-Y. Jang, S. J. Kim, S.-P. Cho, M. H. Lee, J. H. Heo, J. Park, Y. Ko, S. K. Park, J. Kim, K. Oh, D.-H. Kim, S. J. Kang and K. Kang, Coupling Structural Evolution and Oxygen-Redox Electrochemistry in Layered Transition Metal Oxides, *Nat. Mater.*, 2022, **21**, 664–672.

20 D. A. Kitchaev, J. Vinckeviciute and A. Van der Ven, Delocalized Metal–Oxygen π-Redox Is the Origin of Anomalous Nonhysteretic Capacity in Li-Ion and Na-Ion Cathode Materials, *J. Am. Chem. Soc.*, 2021, **143**, 1908–1916.

21 J. H. Song, G. Yoon, B. Kim, D. Eum, H. Park, D. H. Kim and K. Kang, Anionic Redox Activity Regulated by Transition Metal in Lithium-Rich Layered Oxides, *Adv. Energy Mater.*, 2020, **10**, 2001207.

22 M. Okubo and A. Yamada, Molecular Orbital Principles of Oxygen-Redox Battery Electrodes, *ACS Appl. Mater. Interfaces*, 2017, **9**, 36463–36472.

23 T. Sudayama, K. Uehara, T. Mukai, D. Asakura, X.-M. Shi, A. Tsuchimoto, B. Mortemard de Boisse, T. Shimada, E. Watanabe, Y. Harada, M. Nakayama, M. Okubo and A. Yamada, Multiorbital Bond Formation for Stable Oxygen-Redox Reaction in Battery Electrodes, *Energy Environ. Sci.*, 2020, **13**, 1492–1500.

24 A. Tang, R. Zhao, Y. Wu, C. Wan, Z. Li, X. Meng, K. Sun, R. Li, H. Zhang, D. Chen and X. Ju, Ligand-to-Metal Charge Transfer Motivated the Whole-Voltage-Range Anionic Redox in P2-Type Layered Oxide Cathodes, *Adv. Funct. Mater.*, 2024, **34**, 2402639.

25 K. Zhang, Z. Jiang, F. Ning, B. Li, H. Shang, J. Song, Y. Zuo, T. Yang, G. Feng, X. Ai and D. Xia, Metal-Ligand π Interactions in Lithium-Rich Li_2RhO_3 Cathode Material Activate Bimodal Anionic Redox, *Adv. Energy Mater.*, 2021, **11**, 2100892.

26 M.-H. Kim, H. Jang, E. Lee, J. Seo, J. Park, A. Choi, T. Kim, M. Choi, E. Kim, Y. H. Jung, S. J. Kang, J. Cho, Y. Li, M. G. Kim, D.-H. Seo and H.-W. Lee, Metal-to-Metal Charge Transfer for Stabilizing High-Voltage Redox in Lithium-Rich Layered Oxide Cathodes, *Sci. Adv.*, 2025, **11**, eadt0232.

27 R. G. Burns, *Mineralogical Applications of Crystal Field Theory*, Cambridge University Press, Cambridge, 2 edn, 1993.

28 B. Mortemard de Boisse, G. Liu, J. Ma, S.-i. Nishimura, S.-C. Chung, H. Kiuchi, Y. Harada, J. Kikkawa, Y. Kobayashi, M. Okubo and A. Yamada, Intermediate

Honeycomb Ordering to Trigger Oxygen Redox Chemistry in Layered Battery Electrode, *Nat. Commun.*, 2016, **7**, 11397.

29 X. Cao, H. Li, Y. Qiao, X. Li, M. Jia, J. Cabana and H. Zhou, Stabilizing Reversible Oxygen Redox Chemistry in Layered Oxides for Sodium-Ion Batteries, *Adv. Energy Mater.*, 2020, **10**, 1903785.

30 X. Cai, N. Wang, L. Liang, X.-L. Li, R. Zhang, L. Ma, E. Hu, S. Shen, Z. Shadike and J. Zhang, Fast Oxygen Redox Kinetics Induced by CoO_6 Octahedron With π-Interaction in P2-Type Sodium Oxides, *Adv. Funct. Mater.*, 2024, **34**, 2409732.

31 S. M. Kang, D. Kim, K. S. Lee, M. S. Kim, A. Jin, J. H. Park, C. Y. Ahn, T. Y. Jeon, Y. H. Jung, S. H. Yu, J. Mun and Y. E. Sung, Structural and Thermodynamic Understandings in Mn-Based Sodium Layered Oxides during Anionic Redox, *Adv. Sci.*, 2020, **7**, 2001263.

32 J. W. Somerville, A. Sobkowiak, N. Tapia-Ruiz, J. Billaud, J. G. Lozano, R. A. House, L. C. Gallington, T. Ericsson, L. Häggström, M. R. Roberts, U. Maitra and P. G. Bruce, Nature of the "Z"-Phase in Layered Na-Ion Battery Cathodes, *Energy Environ. Sci.*, 2019, **12**, 2223.

33 X. Cai, Z. Shadike, N. Wang, X.-L. Li, Y. Wang, Q. Zheng, Y. Zhang, W. Lin, L. Li, L. Chen, S. Shen, E. Hu, Y.-N. Zhou and J. Zhang, Constraining Interlayer Slipping in P2-Type Layered Oxides with Oxygen Redox by Constructing Strong Covalent Bonds, *J. Am. Chem. Soc.*, 2025, **147**, 5860–5870.

34 T. Zhang, M. Ren, Y. Huang, F. Li, W. Hua, S. Indris and F. Li, Negative Lattice Expansion in an O3-Type Transition-Metal Oxide Cathode for Highly Stable Sodium-Ion Batteries, *Angew. Chem., Int. Ed.*, 2024, **63**, e202316949.

35 X. Liu, W. Zuo, B. Zheng, Y. Xiang, K. Zhou, Z. Xiao, P. Shan, J. Shi, Q. Li, G. Zhong, R. Fu and Y. Yang, P2-$Na_{0.67}Al_xMn_{1-x}O_2$: Cost-Effective, Stable and High-Rate Sodium Electrodes by Suppressing Phase Transitions and Enhancing Sodium Cation Mobility, *Angew. Chem., Int. Ed.*, 2019, **58**, 18086–18095.

36 L. Sun, Z. Wu, M. Hou, Y. Ni, H. Sun, P. Jiao, H. Li, W. Zhang, L. Zhang, K. Zhang, F. Cheng and J. Chen, Unraveling and Suppressing the Voltage Decay of High-Capacity Cathode Materials for Sodium-Ion Batteries, *Energy Environ. Sci.*, 2024, **17**, 210–218.

37 Z. Zhuo, C. D. Pemmaraju, J. Vinson, C. Jia, B. Moritz, I. Lee, S. Sallies, Q. Li, J. Wu, K. Dai, Y.-d. Chuang, Z. Hussain, F. Pan, T. P. Devereaux and W. Yang, Spectroscopic Signature of Oxidized Oxygen States in Peroxides, *J. Phys. Chem. Lett.*, 2018, **9**, 6378–6384.

38 Z. Zhuo, Y.-s. Liu, J. Guo, Y.-d. Chuang, F. Pan and W. Yang, Full Energy Range Resonant Inelastic X-ray Scattering of O_2 and CO_2: Direct Comparison with Oxygen Redox State in Batteries, *J. Phys. Chem. Lett.*, 2020, **11**, 2618–2623.

39 B. Wang, Z. Zhuo, H. Li, S. Liu, S. Zhao, X. Zhang, J. Liu, D. Xiao, W. Yang and H. Yu, Stacking Faults Inducing Oxygen Anion Activities in Li_2MnO_3, *Adv. Mater.*, 2023, **35**, 2207904.

40 S. Roychoudhury, R. Qiao, Z. Zhuo, Q. Li, Y. Lyu, J.-H. Kim, J. Liu, E. Lee, B. J. Polzin, J. Guo, S. Yan, Y. Hu, H. Li, D. Prendergast and W. Yang, Deciphering the Oxygen

Absorption Pre-edge: A Caveat on its Application for Probing Oxygen Redox Reactions in Batteries, *Energy Environ. Sci.*, 2021, **4**, 246–254.

41 K. Dai, J. Wu, Z. Zhuo, Q. Li, S. Sallis, J. Mao, G. Ai, C. Sun, Z. Li, W. E. Gent, W. C. Chueh, Y.-d. Chuang, R. Zeng, Z.-x. Shen, F. Pan, S. Yan, L. F. J. Piper, Z. Hussain, G. Liu and W. Yang, High Reversibility of Lattice Oxygen Redox Quantified by Direct Bulk Probes of Both Anionic and Cationic Redox Reactions, *Joule*, 2019, **3**, 518–541.

42 C. Cheng, S. Li, T. Liu, Y. Xia, L.-Y. Chang, Y. Yan, M. Ding, Y. Hu, J. Wu, J. Guo and L. Zhang, Elucidation of Anionic and Cationic Redox Reactions in a Prototype Sodium-Layered Oxide Cathode, *ACS Appl. Mater. Interfaces*, 2019, **11**, 41304–41312.

43 X. Gao, B. Li, K. Kummer, A. Geondzhian, D. A. Aksyonov, R. Dedryvère, D. Foix, G. Rousse, M. Ben Yahia, M.-L. Doublet, A. M. Abakumov and J.-M. Tarascon, Clarifying the Origin of Molecular O_2 in Cathode Oxides, *Nat. Mater.*, 2025, **24**, 743–752.

44 S. S. Manoharan and R. K. Sahu, Evidence for an Anomalous Redox Ionic Pair between Ru and Mn in $SrRu_{0.5}Mn_{0.5}O_3$: An X-ray Absorption Spectroscopy Approach, *Chem. Commun.*, 2002, 3068–3069.

45 X. Xia, T. Liu, C. Cheng, H. Li, T. Yan, H. Hu, Y. Shen, H. Ju, T. S. Chan, Z. Wu, Y. Su, Y. Zhao, D. Cao and L. Zhang, Suppressing the Dynamic Oxygen Evolution of Sodium Layered Cathodes through Synergistic Surface Dielectric Polarization and Bulk Site-Selective Co-Doping, *Adv. Mater.*, 2023, **35**, e2209556.

46 C. Cheng, M. Ding, T. Yan, J. Jiang, J. Mao, X. Feng, T.-S. Chan, N. Li and L. Zhang, Anionic Redox Activities Boosted by Aluminum Doping in Layered Sodium-Ion Battery Electrode, *Small Methods*, 2022, **6**, 2101524.

47 H. Hu, H.-C. He, R.-K. Xie, C. Cheng, T. Yan, C. Chen, D. Sun, T.-S. Chan, J. Wu and L. Zhang, Achieving Reversible Mn^{2+}/Mn^{4+} Double Redox Couple through Anionic Substitution in a P2-Type Layered Oxide Cathode, *Nano Energy*, 2022, **99**, 107390.

48 J. Wu, Z. Zhuo, X. Rong, K. Dai, Z. Lebens-Higgins, S. Sallis, F. Pan, L. F. J. Piper, G. Liu, Y.-D. Chuang, Z. Hussain, Q. Li, R. Zeng, Z.-X. Shen and W. Yang, Dissociate Lattice Oxygen Redox Reactions from Capacity and Voltage Drops of Battery Electrodes, *Sci. Adv.*, 2020, **6**, eaaw3871.

49 E. Talaie, S. Y. Kim, N. Chen and L. F. Nazar, Structural Evolution and Redox Processes Involved in the Electrochemical Cycling of P2-$Na_{0.67}[Mn_{0.66}Fe_{0.20}Cu_{0.14}]O_2$, *Chem. Mater.*, 2017, **29**, 6684–6697.

50 L. Yang, X. Li, J. Liu, S. Xiong, X. Ma, P. Liu, J. Bai, W. Xu, Y. Tang, Y.-Y. Hu, M. Liu and H. Chen, Lithium-Doping Stabilized High-Performance P2-$Na_{0.66}Li_{0.18}Fe_{0.12}Mn_{0.7}O_2$ Cathode for Sodium Ion Batteries, *J. Am. Chem. Soc.*, 2019, **141**, 6680–6689.

51 S. He, R. Zhang, X. Han, Y. Zhou, C. Zheng, C. Li, X. Xue, Y. Chen, Z. Wu, J. Gan, L. She, F. Qi, Y. Liu, M. Zhang, W. Du, Y. Jiang, M. Gao and H. Pan, Unraveling 3d Transition Metal (Ni, Co, Mn, Fe, Cr, V) Ions Migration in

Layered Oxide Cathodes: A Pathway to Superior Li-Ion and Na-Ion Battery Cathodes, *Adv. Mater.*, 2025, 2413760.

52 C. Cheng, C. Chen, S. Chu, H. Hu, T. Yan, X. Xia, X. Feng, J. Guo, D. Sun, J. Wu, S. Guo and L. Zhang, Enhancing the Reversibility of Lattice Oxygen Redox Through Modulated Transition Metal–Oxygen Covalency for Layered Battery Electrodes, *Adv. Mater.*, 2022, **34**, 2201152.